Applied Catalysis B: Environment and Energy 375 (2025) 125429

Contents lists available at ScienceDirect

Applied Catalysis B: Environment and Energy

journal homepage: www.elsevier.com/locate/apcatb

Designing and understanding efficient catalysts for CO_2 hydrogenation to ethanol on trinuclear Cu-ZSM-5 frameworks

Chaomin Chen [a,b], Jurij Golobič [a,d], Žan Lavrič [a,b], Blaž Likozar [a,*], Matej Huš [a,c,**]

[a] National Institute of Chemistry, Department of Catalysis and Chemical Reaction Engineering, Hajdrihova 19, Ljubljana SI-1001, Slovenia
[b] University of Nova Gorica, Vipavska 13, Nova Gorica 5000, Slovenia
[c] Association for Technical Culture of Slovenia (ZOTKS), Zaloška 65, Ljubljana SI-1001, Slovenia
[d] University of Maribor, Smetanova 17, Maribor 2000, Slovenia

ARTICLE INFO

Keywords:
CO_2 hydrogenation
Ethanol
Trinuclear Cu-ZSM-5
Microkinetic modeling
DFT

ABSTRACT

CO_2 hydrogenation to ethanol is an attractive strategy to mitigate greenhouse gas emissions while producing easily useful fuels. In this study, we perform a comprehensive *ab initio* multiscale study combining density functional theory and a microkinetic batch reactor modelling to elucidate the mechanism of ethanol formation via CO_2 hydrogenation over a trinuclear Cu-ZSM-5 catalyst. Two different zeolite framework configurations (-Al-Si-Al- and -Al-Si-Si-Al-) are systematically investigated to identify bi-substituted sites. Then, a stable trinuclear Cu-ZSM-5 model is found by structural optimization and copper coordination analysis. Subsequent investigation of the adsorption modes of reactive species reveals the complete reaction pathway, with the explicit determination of all listed elementary steps and associated energy barriers. By implementing these findings into a coupled microkinetic framework, we establish 250 °C as the optimal temperature for ethanol production. Additionally, a stoichiometric H_2/CO_2 ratio of 3:1 is identified as the most effective condition to enhance ethanol synthesis. The derived results exhibit strong agreement with previous theoretical studies on analogous systems and show remarkable agreement with experimental observations, conclusively confirming the superior catalytic activity of trinuclear Cu-ZSM-5 in this reaction system.

1. Introduction

The rapid pace of industrialization has greatly increased greenhouse gas emissions from the burning of fossil fuels and other sources, presenting a major challenge to human society. The most important greenhouse gas, carbon dioxide (CO_2), is still being emitted, which led to extreme climate events around the whole world [1]. Reducing CO_2 emissions and promoting sustainable development are urgent issues to be resolved. Current strategies to reduce CO_2 levels in the atmosphere mainly include carbon capture, utilization and storage [2]. Converting CO_2 into higher value chemicals such as hydrocarbons, alcohols, carbonates and oxygenated acid salts is being used to mitigate this problem [3].

Recently, research has focused on the hydrogenation of CO_2 for synthesizing C_1 compounds, such as methanol, carbon monoxide, and methane [1]. On the other hand, a direct conversion of CO_2 into C_{2+} compounds (e.g. ethanol, ethylene) remains a major challenge [4]. Ethanol [5] can be used as a fuel additive or fuel, solvent or platform chemical. The pathway of ethanol production from CO_2 and H_2 involves several steps and includes various intermediates, such as CH_x, CO, HCOOH, COOH, and CH_xO [6]. A good catalyst for the production of C_{2+} compounds must enable CO_2 adsorption and activation, C-C bond formation, and hydrogenation. Achieving high yields and selectivity remains particularly challenging.

Copper (Cu)-based catalysts have garnered much attention due to their high activity in CO_2 hydrogenation and C-C bond formation [7]. Their modifications, such as the introduction of alkali or transition metals, can improve their performance further but Cu remains the foremost metal for C-C coupling [8]. Zeolites, however, possess structural properties that enhance catalytic performance, such high active

* Corresponding author.
** Corresponding author at: National Institute of Chemistry, Department of Catalysis and Chemical Reaction Engineering, Hajdrihova 19, Ljubljana SI-1001, Slovenia.
E-mail addresses: blaz.likozar@ki.si (B. Likozar), matej.hus@ki.si (M. Huš).

https://doi.org/10.1016/j.apcatb.2025.125429
Received 17 February 2025; Received in revised form 18 April 2025; Accepted 30 April 2025
Available online 1 May 2025

surface and porosity [9], and the combination of Cu-based catalysts with zeolites improves their performance. For instance, Ding et al. [10] conducted density functional theory calculations to investigate the formation of the surface methyl group and C–C bonds. In addition, the combination of zeolite structures with copper oxide [11–13] and metallic Cu surfaces [14,15] has also been studied.

Several methods for their synthesis exist, such as hydrothermal synthesis [7,16], ion exchange [17] and others [12,18]. Existing research has primarily focused on mononuclear and binuclear sites, as well as oxygen-bridged copper-oxo clusters [19]. For instance, the decomposition of N_2O over the binuclear Cu active site on the sinusoidal channel of Cu-ZSM-5 has been studied [20]. Furthermore, Cu-ZSM-5-n zeolites possess both the monomeric and binuclear sites and are capable of oxidizing methane to methanol [21]. Compared to binuclear sites, trinuclear could offer several advantages, such as synergistic catalytic effects, enhanced structural flexibility, improved thermodynamic stability, and distinct geometric and electronic structures [22]. Trinuclear Cu-oxygen clusters have been successfully synthesized via ion-exchange method in mordenite for selective methane oxidation reaction [23]. Recent studies have also demonstrated the integration of these clusters in CO_2 photoreduction [24].

While systematic experimental and computational studies on trinuclear copper zeolites remain scarce, coordination environment analyses [7] and anomalous active site identification [10] suggest their existence. Recent advances in CO_2 hydrogenation showcase the role of polynuclear metal synergy for C-C coupling [25,26]. Trinuclear architectures were confirmed by the experimental work of An et al. [7], who introduced a third alkali metal atom in Cu-Zr_{12}-bpdc-CuX (X = Li, Na, K, Rb, Cs), which strongly affected the CO_2 hydrogenation pathways.

Hence, our work is motivated by the disparity between the well-established applications of trinuclear Cu-O clusters [27,28] and the simplified models (e.g., slabs [29] or nanoparticle systems [30]) used in computational studies. These, however, neglect effects inherent to zeolites: confinement and the cooperativity of multinuclear active centers. In our study, we systematically analyzed the porous structure of trinuclear Cu-ZSM-5. First, energy analysis was used to determine the Cu substitution sites. Löwenstein's rule [31] was applied to explore two possible scenarios: the -Al-Si-Al- and -Al-Si-Si-Al- configurations, which were used to identify the doubly substituted sites. After considering the structural stability and the coordination of copper atoms, a trinuclear structure was obtained. Subsequently, the adsorption of reactants, intermediates, and products was investigated to evaluate their roles in C–C bond formation and C═O bond cleavage using density functional theory (DFT). The activation and reaction energies for all relevant elementary steps were computed, which were then used in a microkinetic model. It was used to simulate the reaction in various conditions, such as pressure, reaction temperature, and reactant ratios. To assess the kinetic properties, the turnover frequency (TOF) was computed.

To the best of our knowledge, this is the first *ab initio* based multiscale model of CO_2 hydrogenation to ethanol on zeolite catalysts. It provides theoretical understanding of the reaction and provides guidance for its practical applications, while at the same time it serves as proof of concept of *ab initio* multiscale models.

2. Computational methodology

2.1. DFT calculations

All calculations of the periodic density function theory calculations performed with the Grid-based Projector Augmented Wave (GPAW) program [32,33] which is based on the Atomic Simulation Environment (ASE) [34]. The Generalized-Gradient Approximation (GGA) with the Perdew-Burke-Ernzerhof (PBE) exchange-correction functional was used [35]. During the structure optimization and transition state calculations, the electronic density was set to be converged with a threshold value of 10^{-6} eV and the structure was considered optimized when the forces at each atom dropped below 0.03 eV $Å^{-1}$. Dispersion corrections were accounted for using Grimme's DFT-D3 method [36].

PBE-D3 was chosen as a compromise between the computational cost and chemical accuracy due to a relatively large periodic system, consisting of approximately 300 atoms. It is, however, known to overestimate adsorption strength in some instances [37] of smaller cluster (non-periodic) models with fewer atoms.

The energy cutoff for the wave function was set at 520 eV as determined by preliminary convergence tests. The unit cell was sampled using a 1 × 1 × 1 k-point mesh due to the size of the unit cell. Optimizations were performed using the Broyden-Fletcher-Goldfarb-Shanno (BFGS) algorithm [38]. The nudged elastic band (NEB) [39] was employed to identify the transition states (TS), which were further verified with the vibrational analysis to ensure that they contain only one imaginary frequency. During the optimization of the Cu-ZSM-5 model, the electron vacancy created by the substitution of aluminum for silicon is compensated by the introduction of copper, forming a stable active site [40]. All optimized structures were visualized using the VESTA software (Visualization for Electronic and Structure Analysis) [41].

To determine the adsorption energies, the following formula was used:

$$\Delta E_{ads} = E_{adsorbed} - E_{catalyst} - E_{species}$$

where $E_{adsorbed}$ represents the total energy of the system when the species is adsorbed onto the active site, $E_{catalyst}$ is the total energy of the clean catalyst, free from any adsorbed species and $E_{species}$ means the total energy of the isolated species in its most stable form.

The forward activation energy ($E_{a,fwd}$) and reaction energy (ΔE) for each elementary step were determined as follows:

$$E_{a,fwd} = E_{TS} - E_{reactant}$$

$$\Delta E = E_{product} - E_{reactant}$$

In these equations, E_{TS} represents the relative energy of transition state, while $E_{reactant}$ indicates the relative energy of reactant, and $E_{product}$ denotes the relative energy of product.

To evaluate the stability of the reaction intermediates, we compared the changes in the Gibbs free energy [42], which included the vibrational contribution for the adsorbed species and the vibrational, rotational and translational contributions for gaseous species (see below).

$$G_{a,fwd} = G_{TS} - G_{reactant}$$

$$\Delta G = G_{product} - G_{reactant}$$

$$G_{rev} = G_{TS} - G_{product}$$

Here, G_{TS} is the Gibbs free energy of the transition state, $G_{reactant}$ represents the Gibbs free energy of the reactant, and $G_{product}$ refers to the Gibbs free energy of the product. ΔG indicates the Gibbs free energy difference between the product and the reactant. The rate constants of the activated conversion of adsorbed reactant are determined using the conventional transition-state theory (TST) [43]. In TST, the Gibbs free energies of both the adsorbates and the transition state at a given temperature are evaluated based on the harmonic approximation, which allows for the calculation of Gibbs free energy, as follows:

$$k_{fwd} = \frac{k_B * T}{h} \frac{Z'}{Z} e^{-\frac{\Delta E}{k_B * T}}$$

where Z and Z' represent the partition function for the initial state and the transition state, k_B is the Boltzmann constant, T is the temperature, and h is Planck's constant. Partition functions of reactants, transition and products were calculated, taking into account zero-point energy corrections as well as translational, vibrational and rotational motion [44]. These were then used to calculate the enthalpy, entropy and Gibbs

free energy of species, the reaction rate of surface reaction can be expressed by:

$$k_{fwd} = \frac{k_B * T}{h} * e^{-\frac{\Delta G}{k_B * T}}$$

While the reaction rates for reverse reactions k_{rev} follow from the equilibrium constants (K) [45]:

$$K = \frac{k_{fwd}}{k_{rev}} = e^{-\frac{\Delta G}{k_B T}}$$

The reverse reaction rate is computed analogously:

$$k_{rev} = \frac{k_B * T}{h} * e^{-\frac{G_{rev}}{k_B * T}}$$

The calculations were performed across a temperature range of 200–650 °C.

For adsorption reactions, the adsorption is a function of pressure and temperature and is generally non-activated (except for dissociative adsorption of hydrogen):

$$k_{ads} = \frac{p_x * S}{\sqrt{2 * \pi * M_x * k_B * T}}$$

P_x is the partial pressure of species X , S means the surface area of the active site (estimated as 0.1 nm^2), M_x is the mass of the molecule of species X. The reverse reaction represents desorption, which entails an activation barrier, and is computed as:

$$k_{des} = \frac{k_B * T}{h} * e^{\frac{E_{ads}}{k_B * T}}$$

2.2. Microkinetic modelling

To evaluate the DFT data in a realistic scenario, a microkinetic batch reactor model was developed, incorporating all the relevant elementary steps to explore the effects of varying reaction conditions and to predict the kinetics of CO_2 hydrogenation to ethanol. The model considered an ethanol synthesis scheme featuring distinct adsorbate species, gaseous phase reactants and (by-)products, and accounted for the potential by-products, such as methanol. It encompassed all reaction pathways as determined by DFT without assuming a rate-determining step. The rates for surface reactions (k_{fwd}, k_{rev}) and adsorption/desorption reactions (k_{ads}, k_{des}) were directly derived from DFT calculations and the transition state theory without resorting to phenomenological fitting of experimental data. To enhance the model stability and reduce computational times, fast reaction rates were scaled accordingly (stiffness scaling).

In the microkinetic model, the following surface species are considered: CO_2, H_2, H, CO, O, OH, CH_3 (Methyl), t-COOH, c-COOH, HCO (Formyl), H_2CO (Formaldehyde), H_3CO (Methoxy), CH_3CO (Acetyl), CH_3CHO (Acetaldehyde), CH_3CH_2O (Ethoxy), CH_3CH_2OH (Ethanol), H_2O CH_3OH (Methanol). The initial values of the gas composition were varied depending on the concentration range investigated, while no species were bound to the catalyst's surface. As active sites must be either free or covered by an intermediate, the site balance equation must be obeyed:

$$\theta_H + \theta_{CO_2} + \theta_{H_2} + \theta_{CO} + \theta_O + \theta_{OH} + \theta_{CH_3} + \theta_{tCOOH} + \theta_{cCOOH} + \theta_{HCO} + \theta_{H_2CO} + \theta_{H_3CO} + \theta_{CH_3CO} + \theta_{CH_3CHO} + \theta_{CH_3CH_2O} + \theta_{CH_3CH_2OH} + \theta_{H_2O} + \theta_{CH_3OH} + \theta_{Empty} = 1 = \theta_{total}$$

where θ denotes the coverage of a species, θ_{Empty} represent the fraction of free active sites, and the total coverage is always equal to 1. The Cu cluster, where the intermediates adsorb, is considered an active site. For thermodynamic consistency, lateral interactions due to co-adsorption are compensated for in the reaction energies, but their effects are included in the calculation of the activation barriers.

There are 18 surface reactions and 5 adsorption reactions included in the microkinetic model. All the elementary steps and corresponding rate equations are listed in Table 1. In Table 1, p is the partial pressure of the component in the bulk. To reconcile the different units of measurement of gaseous and adsorbed species, the scaling factor of available surface sites must be supplied and used for the former:

$$f = \frac{NRT}{V_{sys}}$$

where N is the number of moles of the active sites on the catalyst and was set as 0.01 mol. R is the universal gas constant, T is the reaction temperature and V_{sys} is the volume of the system (99 mL). The molar balances of all the surface reactions and adsorption reactions are shown in Supporting information.

To replicate these conditions and align with kinetic modeling simulations, our model utilized a batch reactor framework. Simulation parameters were selected to reflect typical experimental setups. The system's behavior was simulated using the SciPy package in Python, employing the LSODA method for its capacity to efficiently manage both stiff and non-stiff systems dynamically.

TOF is defined as the number of catalytic cycles or reactions that take place at each active site per unit of time. For example, the TOF of ethanol can be precisely calculated in theoretical models using the following formula:

$$TOF_{ethanol} = r_{13}$$

It should be noted that the reversible reaction is considered in our model. The maximum value of TOF was used to plot the Arrhenius equation, which is typically used to analyze the temperature dependence of reaction rates, the apparent activation energy can be conducted according to Arrhenius equation:

$$\log TOF = -\frac{E_{apprant}}{R}\left(\frac{1}{T}\right) + \log A$$

where TOF represents the turnover frequency as a measurement of the reaction rate. The slope of Arrhenius plot represents the apparent activation energy ($E_{apparent}$) which provides insight into the temperature dependence of the reaction. However, the activation energy alone does not fully determine the reaction rate, the pre-exponential factor (A) also plays a critical role. Furthermore, different reactions (for instance forming methanol or ethanol) can and usually do reach peak TOF values at different times and cannot be easily compared. Thus, maximum TOF is not a direct measure of the overall selectivity of conversion.

The conversion of reactant is calculated as below:

$$Conversion\ of\ reactant = 1 - \frac{final\ moles\ of\ reactant}{initial\ moles\ of\ reactant}$$

The selectivity of product from reactant is calculated by:

$$Selectivity\ of\ product = \frac{moles\ of\ desired\ product}{moles\ of\ reactant\ consumed}$$

2.3. The zeolite model

The original structure is available for download from the International Zeolite Association (IZA) database [46]. ZSM-5 was selected due to its distinct framework, with a basic unit cell containing 96 Si atoms and 192 O atoms, distributed across 12 crystallographic distinct T sites (T atoms refers to tetrahedrally coordinated Si) and promising catalytic properties [30,47]. In our optimized model (shown in Fig. 1), the lattice parameters of ZSM-5 are (see Table S1): a = 19.68 Å, b = 19.32 Å, and c = 12.88 Å, with angles close to 90°. The structure belongs to the orthorhombic crystal system, with a space group of *Pnma*. The 3D framework consists of straight ten-membered rings (10-MRs) and intersecting 5/6-MRs voids, forming sinusoidal channels. These channels, parallel to the [010] zone axis, corresponding to atomic-resolution

Table 1
Elementary steps and rate equations considered in the Microkinetic Model. Where X (g) denotes a gas component, X* the adsorbed species. All the reactions are considered to be reversible and first order.

	Step	Elementary Reaction	Rate Equation
Surface Reactions	R1	$CO_2^* + H^* \rightleftharpoons t-COOH^* + *$	$r_1 = k1_{fwd} * \theta_{CO_2} * \theta_H - k1_{rev} * \theta_{tCOOH} * \theta_{Empty}$
	R2	$t-COOH^* \rightleftharpoons c-COOH^*$	$r_2 = k2_{fwd} * \theta_{tCOOH} - k2_{rev} * \theta_{cCOOH}$
	R3	$c-COOH^* + * \rightleftharpoons CO^* + OH^*$	$r_3 = k3_{fwd} * \theta_{cCOOH} * \theta_{Empty} - k3_{rev} * \theta_{CO} * \theta_{OH}$
	R4	$CO_2^* + * \rightleftharpoons CO^* + O^*$	$r_4 = k4_{fwd} * \theta_{CO_2} * \theta_{Empty} - k4_{rev} * \theta_{CO} * \theta_O$
	R5	$CO^* + H^* \rightleftharpoons HCO^* + *$	$r_5 = k5_{fwd} * \theta_{CO} * \theta_H - k5_{rev} * \theta_{HCO} * \theta_{Empty}$
	R6	$HCO^* + H^* \rightleftharpoons H_2CO^* + *$	$r_6 = k6_{fwd} * \theta_{HCO} * \theta_H - k6_{rev} * \theta_{H_2CO} * \theta_{Empty}$
	R7	$H_2CO^* + H^* \rightleftharpoons H_3CO^* + *$	$r_7 = k7_{fwd} * \theta_{H_2CO} * \theta_H - k7_{rev} * \theta_{H_3CO} * \theta_{Empty}$
	R8	$H_3CO^* + * \rightleftharpoons H_3C^* + O^*$	$r_8 = k8_{fwd} * \theta_{H_3CO} * \theta_{Empty} - k8_{rev} * \theta_{CH_3} * \theta_O$
	R9	$H_3C^* + CO^* \rightleftharpoons CH_3CO^* + *$	$r_9 = k9_{fwd} * \theta_{CO} * \theta_{CH_3} - k9_{rev} * \theta_{CH_3CO} * \theta_{Empty}$
	R10	$H_3C^* + HCO^* \rightleftharpoons CH_3CHO^* + *$	$r_{10} = k10_{fwd} * \theta_{HCO} * \theta_{CH_3} - k10_{rev} * \theta_{CH_3CHO} * \theta_{Empty}$
	R11	$CH_3CO^* + H^* \rightleftharpoons CH_3CHO^* + *$	$r_{11} = k11_{fwd} * \theta_{CH_3CO} * \theta_H - k11_{rev} * \theta_{CH_3CHO} * \theta_{Empty}$
	R12	$CH_3CHO^* + H^* \rightleftharpoons CH_3CH_2O^* + *$	$r_{12} = k12_{fwd} * \theta_{CH_3CHO} * \theta_H - k12_{rev} * \theta_{CH_3CH_2O} * \theta_{Empty}$
	R13	$CH_3CH_2O^* + H^* \rightleftharpoons CH_3CH_2OH^* + *$	$r_{13} = k13_{fwd} * \theta_{CH_3CH_2O} * \theta_H - k13_{rev} * \theta_{CH_3CH_2OH} * \theta_{Empty}$
	R14	$OH^* + H^* \rightleftharpoons H_2O^* + *$	$r_{14} = k14_{fwd} * \theta_{OH} * \theta_H - k14_{rev} * \theta_{H_2O} * \theta_{Empty}$
	R15	$H_2^* + * \rightleftharpoons H^* + H^*$	$r_{15} = k15_{fwd} * \theta_{Empty} * \theta_{H_2} - k15_{rev} * \theta_H * \theta_H$
	R16	$O^* + H^* \rightleftharpoons OH^* + *$	$r_{16} = k16_{fwd} * \theta_O * \theta_H - k16_{rev} * \theta_{OH} * \theta_{Empty}$
	R17	$H_3CO^* + H^* \rightleftharpoons CH_3OH^* + *$	$r_{17} = k17_{fwd} * \theta_{H_3CO} * \theta_H - k17_{rev} * \theta_{CH_3OH} * \theta_{Empty}$
	R18	$CH_3OH^* + * \rightleftharpoons CH_3^* + OH^*$	$r_{18} = k18_{fwd} * \theta_{CH_3OH} * \theta_{Empty} - k18_{rev} * \theta_{CH_3} * \theta_{OH}$
Adsorption Reactions	R01	$CO_2 \ (g) + * \rightleftharpoons CO_2^*$	$r_{01} = k01_{ads} * \theta_{Empty} * \theta_{p\_CO_2} - k01_{des} * \theta_{CO_2}$
	R02	$H_2 \ (g) + * \rightleftharpoons H_2^*$	$r_{02} = k02_{ads} * \theta_{Empty} * \theta_{p\_H_2} - k02_{des} * \theta_{H_2}$
	R03	$CH_3CH_2OH^* \rightleftharpoons CH_3CH_2OH(g) + *$	$r_{03} = k03_{ads} * \theta_{CH_3CH_2OH} - k03_{des} * \theta_{Empty} * \theta_{p\_CH_3CH_2OH}$
	R04	$H_2O^* \rightleftharpoons H_2O(g) + *$	$r_{04} = k04_{ads} * \theta_{H_2O} - k04_{des} * \theta_{Empty} * \theta_{p\_H_2O}$
	R05	$CH_3OH^* \rightleftharpoons CH_3OH(g) + *$	$r_{05} = k05_{ads} * \theta_{CH_3OH} - k05_{des} * \theta_{Empty} * \theta_{p\_CH_3OH}$

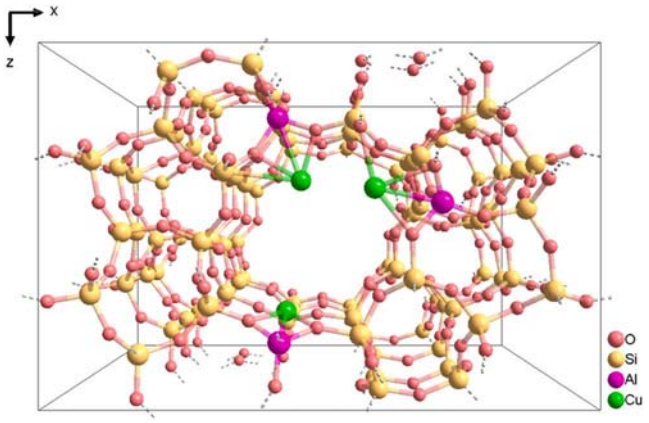

Fig. 1. Schematic structure of the optimized trinuclear Cu-ZSM-5 crystal structure.

images of pure ZSM-5 zeolite along this axis [48]. Such structural characteristics are crucial in determining ZSM-5's catalytic behavior and selectivity.

5- and 6-MRs are often discussed as ways to introduce Cu into the ZSM-5 structure. In our case, we choose the 10-MR ring because it is accessible for the molecular size of both the reactant and the product. For the reactions involving small molecules, 5- and 6-MRs have also been investigated before [49,50], but 10-MR is also investigated [51]. For reactions involving large molecules, such as methanol, the 10-MR rings have been reported more favorable [21,30,52]. Since the T1-T12 sites in ZSM-5 are located in different ring structures, some sites are linked to straight channels and some are linked to adjacent sinusoidal channels. For example, T1 in the sinusoidal channel belongs to β-6MR and 5MR, T9 located in the sinusoidal channel belongs to γ-6MR, T8 are included in both β-6MR and δ-5MR [53]. The location of the T site prompted us to favor the -Al-Si-Al- and -Al-Si-Si-Al- configurations within the 10-MR over more complex configurations (e.g., -Al-Si-Si--Si-Al-, -Al-Si-Si-Si-Si-Al-) due to computational constraints. Once the binuclear system was established, a third metal atom was added.

3. Results

3.1. Active site

To model the active site, the substitution sites were selected according to Löwenstein's rule [31], which states that Al–O–Al bond formation is forbidden. In our work, we primarily determined to introduce two Cu atoms as active sites and calculated the possible replacement sites based on our configurations these substitution energies correspond to Dai's work [21]. For single substitutions, as shown in Fig. S1, the T11 site exhibits the lowest energy configuration, indicating its potential as the most stable and effective catalytic site. In this case, however, a single Cu-based catalyst has the limitation of hydrogenation ability and weak carbon-chain extension ability in the synthesis of C_{2+}. On account of the specific function of Cu-based catalysts for alcohols production, an approximate amount of Cu atoms was impregnated and used as catalysts to produce C_{2+} products, including the formations of alcohols [5]. For the double substitution cases, two scenarios were explored: the -Al-Si-Al- pattern and the -Al-Si-Si-Al- configuration. As illustrated in Fig. S2, within the -Al-Si-Al- pattern, the T3T11 site combination demonstrated the lowest energy, implying great stability and catalytic potential. In the case of -Al-Si-Si-Al- configurations, the T2T11 combination emerged as the most energetically favorable, as depicted in Fig. S3.

Apart from the energy considerations, the spacing between active sites plays a crucial role in influencing the adsorption of reactants and the reaction pathways. It has been reported that the minimum distance between two adjacent active centers is only 2.7 Å [7]. To enhance the coordination of the dimeric Cu species, it is crucial to maximize the number of the Al pairs in the zeolite that exhibit the optimal Al-Al distance [54]. Considering these spatial constraints, we explored alternative configurations. Both the substitution energy and the distance between copper active site were simultaneously evaluated and shown in Table 2. Five possible configurations for the double substitution were selected for further investigation, leading to the introduction of a third atom to catalyze the final formation of chain growth, as demonstrated in Fig. 2.

Our calculations revealed that the T3T5T7 configuration, which incorporates an additional atom following the double substitution results, emerges as the most stable structure. This arrangement strikes a balance

Table 2
Relative energy of various doubly substituted T sites and distances between the active sites, reported relative to the substitution energy for T2T6.

-Al-Si-Al-	Energy (eV)	Distance (Å)	-Al-Si-Si-Al-	Energy (eV)	Distance (Å)
T1T3	− 0.73	3.48	T1T12	− 0.23	3.16
T1T6	− 0.52	2.49	T1T9	− 0.56	2.58
T2T12	− 0.26	2.42	T2T11	− 0.71	2.48
T2T5	− 0.42	2.48	T2T6	0	3.86
T3T11	− 1.33	2.58	T3T7	− 0.69	3.50
T7T12	− 0.53	2.60	T3T5	− 0.42	4.12
T8T11	− 0.86	2.57	T8T12	− 0.48	4.09
T7T9	− 0.69	2.41	T9T11	− 0.48	4.41
T6T8	− 0.21	2.76	T6T7	− 0.01	3.90
T5T9	− 0.60	2.54	T5T8	− 0.42	2.63

between the stability and optimal spacing for efficient adsorption and reaction pathways. Table S2 presents the distances between copper active site and aluminum atoms, along with the corresponding energy for each configuration. Considering the energy and coordination of the copper active site, the T3T5T7 trinuclear Cu-ZSM-5 configuration is established as both energetically feasible and catalytically active.

3.2. Adsorption

Adsorption of all species involved in the reaction was studied. Fig. 3 presents the optimized geometric parameters, adsorption distances and binding energies of the reaction intermediates in their most stable configurations on the trinuclear Cu-ZSM-5 zeolite structure. The atomic coordinates for the optimized trinuclear Cu-ZSM-5 and CO_2, H_2, CH_3CH_2OH and H_2O adsorbed in trinuclear Cu-ZSM-5 are listed in Tables S3–S7. All these adsorption energies are negative, consistent with fundamental thermodynamic principles. For adsorption to be spontaneous, however, it must also exhibit negative Gibbs free energy [55]. When the molecules lose degrees of freedom during the adsorption process, the entropy of the system decreases, which means that more energy is needed to reach the condition of a negative Gibbs free energy, making adsorption less favorable at higher temperatures.

For single atoms, Oxygen (O) shows a strong adsorption energy of − 8.16 eV. The oxygen atom coordinates with three Cu atoms with Cu–O bond distances of 1.83 Å, 1.83 Å, and 1.85 Å. The adsorption energy of hydrogen (H) is − 4.85 eV, Cu–H bond distances of 1.66 Å, 1.69 Å, and 1.73 Å is shown to make this interaction important for the hydrogenation processes. Hydroxyl (CO) also exhibit a strong adsorption energy of − 5.8 eV. its oxygen atom coordinates with three Cu atoms at Cu-O distances of 1.94 Å, 1.96 Å, and 2.02 Å, while the O–H bond length is 0.99 Å.

The important reactant, CO_2, showing a different adsorption mode. The carbon atom is bound to one copper atom, while two oxygen atoms are bound to another two copper atoms in a bent angle of 130°, reveals a strong activation in this configuration. The Cu–C bong length is measured to be 1.88 Å, with Cu–O bond distances of 1.86 Å and 1.91 Å, and C–O bond lengths are 1.27 and 1.26 Å, respectively. This adsorption geometry indicates a strong interaction with adsorption energy of − 1.33 eV. The other important reactant, H_2, is adsorbed on one copper site with the adsorption energy of − 1.31 eV and the Cu-H distances are 1.60 and 1.59 Å. The H–H bond length is 0.87 eV.

CO coordinates with two Cu atoms with the Cu-C distances of 1.89 Å and a Cu-O distance of 1.77 Å. The adsorption energy of − 2.83 eV indicate efficient catalytic reactions involving CO. Methyl binds to two copper atoms as well, mainly by the carbon atom with a Cu–C bond length of 1.98 Å with neighboring Cu atoms interacting with carbon at atomic distance of 2.04 Å.

Carboxyl species, t-COOH and c-COOH, strongly adsorbed on with energies of − 4.26 eV and − 4.62 eV, respectively. The c-COOH isomer binds to a third copper atom through its oxygen atoms due to its different bond angle compared to t-COOH. As the product of CO hydrogenation, HCO coordinates through binding to two Cu atoms, with Cu-C distances of 1.85 Å and a Cu-O distance of 1.83 Å, and an adsorption energy of − 3.83 eV. Formaldehyde (H_2CO) plays a critical role as an intermediate hydrogenation stages, with an adsorption energy of − 2.72 eV. The adsorption energy of Methoxy (H_3CO) is − 4.58 eV.

CH_3CO, a crucial intermediate for ethanol synthesis, interact with one copper atom through its α-carbon atom (Cu-C distance of 1.87 Å) and with another copper atom through its oxygen atom (Cu-O distance of 1.84 Å)., this strong interaction is essential with an adsorption energy of − 4.13 eV for its involvement in further hydrogenation reactions. CH_3CHO adsorbs via its oxygen atom across the two Cu atoms, with Cu–O bond lengths of 1.94 Å and 2.04 Å. CH_3CH_2O adsorbs with its oxygen atom bridging the two Cu atoms at the Cu-O distances of 1.88 Å and 1.92 Å with an adsorption energy of − 4.87 eV.

Ethanol, as the end product of CO_2 hydrogenation, adsorptions occurs through the oxygen atom with Cu–O bond lengths of 2.05 Å and 2.11 Å, and an adsorption energy of − 2.8 eV. Methanol shows a weaker interaction with an adsorption energy of − 2.4 eV. Water, which also forms, exhibits a Cu-O distance at 2.1 Å and an O-H distance of 0.99 Å and an adsorption energy of − 2.00 eV. We see that the interaction in the homologous series increases as the carbon chain is increased.

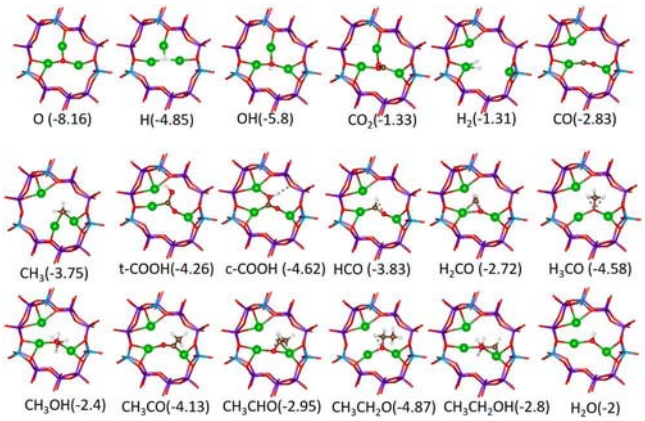

Fig. 3. Adsorption energies of all possible species in the CO_2 hydrogenation process to ethanol. Color-coded of silicon (Si), aluminum (Al), copper (Cu), copper (O), carbon (C) and hydrogen (H) atoms are shown in purple, light blue, green, red, brown and white, respectively. Binding energies are reported in eV.

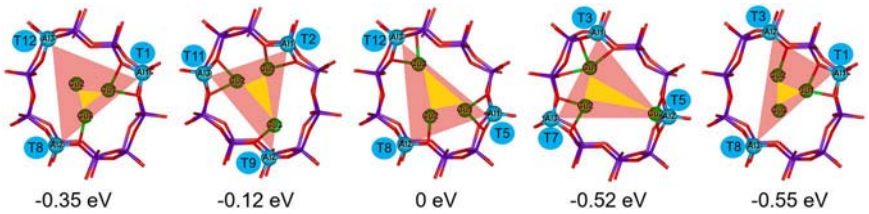

Fig. 2. Optimized structures of five distinct trinuclear Cu-ZSM-5 frameworks and their relative substitution energies. Energies are given relative to the most stable configuration. The relative substitution energy for T5T8T12 is referred as 0.

3.3. Reaction pathway

A comprehensive understanding of reaction mechanism is essential in heterogeneous catalysis, both to develop and utilize catalysts [56]. The catalytic pathway for ethanol synthesis through CO_2 hydrogenation is much more complex than the mechanism of simple hydrogenation to C1 products due to the necessary carbon-carbon (C–C) bond formation [57]. Based on existing reports, we focused on the two primary pathways for CO_2 activation: the redox mechanism ($CO_2^* \rightarrow CO^* + O^*$) and the carboxyl mechanism ($CO_2^* + H^* \rightarrow COOH^*$) [58]. Based on these mechanisms, a simplified reaction network was constructed to describe the formation of C_2 species - ethanol, as illustrated in Fig. 4.

In the proposed reaction pathway, CO is the primary product of CO_2 activation and reduction. Ethanol synthesis then begins with the hydrogenation of CO to HCO. The HCO intermediate undergoes further hydrogenation, yielding H_3CO via the H_2CO intermediate, which can subsequently convert into the by-product CH_3OH. Alternatively, H_3CO can dissociate to form CH_3. The insertion of another molecule of HCO into CH_3 generates the critical intermediate CH_3CHO [59], which is then hydrogenated to produce ethanol through the CH_3CH_2O intermediate. This pathway provides a structured framework for understanding the synthesis mechanism and catalytic behavior in ethanol production.

The elementary steps, detailed in Table 3, alongside with their respective energies offer critical insights into the reaction kinetics and thermodynamics underlying the process. For each elementary step, the structure of initial, transition, and final states are illustrated in Figs. S4–6. To describe the reaction kinetics at various temperature, Gibbs free energies were also calculated, which serve to clarify the thermodynamically favorability of each reaction step. Reactions exhibiting negative Gibbs free energy values are thermodynamically favorable, while positive values denote thermodynamically unfavorable reactions [60]. Furthermore, intermediates characterized by lower Gibbs free energy values indicate increased stability, whereas intermediates with higher Gibbs free energy values are comparatively less stable.

3.3.1. CO formation

The formation of the t-COOH* intermediate (step R1) from CO_2 hydrogenation pathway presents a bottleneck with a relatively high activation energy (2.22 eV). Nevertheless, a negative change in Gibbs free energy of − 0.34 eV is exhibited, indicating that this reaction is thermodynamically favorable and kinetically accessible at high temperatures. Subsequently, steps R2 and R3 are fast with moderately low barriers, which together form a feasible and favorable progression along the t-COOH* pathway. In contrast, the alternative pathway leading to direct CO formation (step R4) requires a lower activation energy (1.54 eV) compared to the initial t-COOH* formation in R1 but a prohibitively positive reaction energy (1.39 eV), making the step thermodynamically unlikely. Thus, the t-COOH* formation pathway (R1–R3) is overall more thermodynamically favorable. The redox pathway (R4), due to its lower activation energy, could be more favorable kinetically at extremely high temperatures, which are otherwise inappropriate for this process.

Table 3
Activation and Gibbs free energy for elementary reaction steps on trinuclear Cu-ZSM-5 under the temperature of 300 °C.

Step	Elementary reaction	E_a, fwd (eV)	G_a, fwd (eV)	ΔE (eV)	ΔG (eV)
R1	$CO_2^* + H^* \rightleftharpoons t-COOH^* + *$	2.22	0.67	0.31	− 0.34
R2	$t-COOH^* \rightleftharpoons c-COOH^*$	0.47	0.40	− 0.24	− 0.21
R3	$c-COOH^* + * \rightleftharpoons CO^* + OH^*$	0.68	0.58	0.03	− 0.04
R4	$CO_2^* + * \rightleftharpoons CO^* + O^*$	1.54	1.47	1.40	1.39
R5	$CO^* + H^* \rightleftharpoons HCO^* + *$	0.64	0.61	0.28	0.37
R6	$HCO^* + H^* \rightleftharpoons H_2CO^* + *$	0.15	0.17	− 0.29	− 0.15
R7	$H_2CO^* + H^* \rightleftharpoons H_3CO^* + *$	0.80	0.67	− 0.06	0.07
R8	$H_3CO^* + * \rightleftharpoons H_3C^* + O^*$	1.82	1.65	1.58	1.53
R9	$H_3C^* + CO^* \rightleftharpoons CH_3CO^* + *$	0.19	0.18	− 1.25	− 1.22
R10	$H_3C^* + CHO^* \rightleftharpoons CH_3CHO^* + *$	0.11	0.13	− 1.28	− 1.26
R11	$CH_3CO^* + H^* \rightleftharpoons CH_3CHO^* + *$	0.88	0.80	− 0.62	− 0.50
R12	$CH_3CHO^* + H^* \rightleftharpoons CH_3CH_2O^* + *$	1.01	0.83	0.24	0.28
R13	$CH_3CH_2O^* + H^* \rightleftharpoons CH_3CH_2OH^* + *$	0.39	0.35	− 0.44	− 0.31
R14	$OH^* + H^* \rightleftharpoons H_2O^* + *$	0.43	0.38	− 0.12	− 0.01
R15	$H_2^* + * \rightleftharpoons H^* + H^*$	0.10	0.01	− 0.08	− 0.13
R16	$O^* + H^* \rightleftharpoons OH^* + *$	0.11	0.03	− 1.65	− 1.59
R17	$H_3CO^* + H^* \rightleftharpoons CH_3OH^* + *$	0.43	0.38	− 0.33	− 0.16
R18	$CH_3OH^* + * \rightleftharpoons CH_3^* + OH^*$	0.86	0.81	0.40	0.33

3.3.2. C1 hydrogenation

Steps R5 and R6, which involve the hydrogenation of CO* and HCO*, are both thermodynamically and kinetically favorable, indicating a

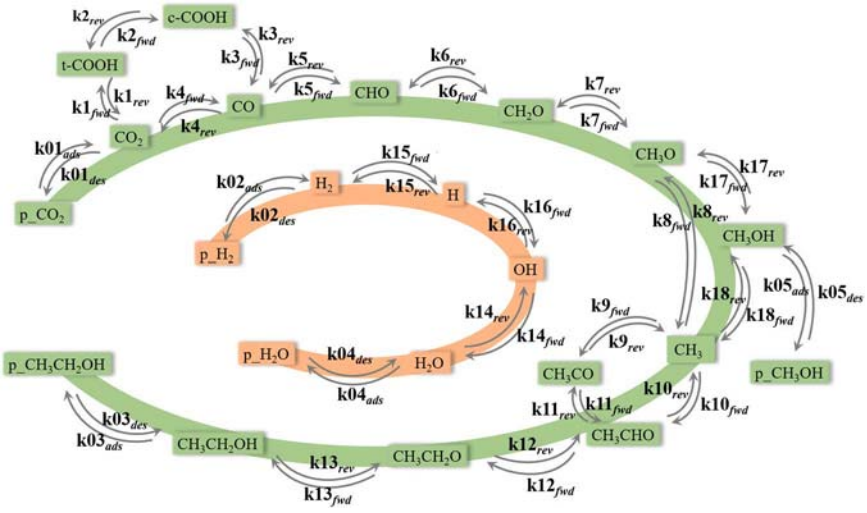

Fig. 4. A scheme of reaction mechanism of CO_2 hydrogenation to ethanol. Only principal intermediates are shown, while balancing H*, OH*, O* and H_2O* are omitted for clarity.

smooth progress in these early hydrogenation steps. Step R7 is feasible but thermodynamically less favorable. Step R17 hydrogenate H_3CO^* to CH_3OH^*, which is also favorable with a moderate activation energy (0.43 eV) and a negative Gibbs free energy (-0.16 eV), and thus methanol formation can be promoted as a possible by-product. Step R8, where H_3CO^* dissociates into H_3C^* and O^*, has a high activation energy and Gibbs free energy values (1.82 eV and 1.65 eV, respectively), this makes it both kinetically and thermodynamically unfavorable and creating a second bottleneck in the reaction sequence (which is responsible for subsequent formation of C–C bond). Instead, H_3C^* can also be formed from the dissociation of CH_3OH^* in R18, especially since its adsorption energy is strong enough to prevent immediate desorption. The reaction (R18) has a positive Gibbs free energy (0.86 eV), indicating that methanol dissociation requires high temperatures and could be another limiting factor for product conversion.

3.3.3. C2 formation

For the C-C coupling process, the competitive pathways are illustrated by reactions R9 and R10, along with the following reaction R11. In R9, the coupling exhibits a low activation energy of 0.19 eV and a Gibbs free energy of activation of 0.18 eV, showing a rapid reaction rate and significant kinetic favorability, with a Gibbs free energy change of − 1.22 eV which is highly exothermic. R10 presents an even lower activation energy of 0.11 eV and a Gibbs free energy of activation of 0.13 eV, improving its kinetic favorability and allowing it to compete efficiently with R9, despite its less exothermic reaction energy change of − 1.26 eV. under operational conditions, both reactions occur simultaneously. R11, following R9, has activation energy of 0.88 eV and a Gibbs free energy of activation of 0.80 eV, meaning that overall R10 is more likely, while R9 and R11 remain side reactions at typical reaction conditions.

In R12, CH_3CHO react with one hydrogen to form CH_3CH_2O, and followingly reacts with second hydrogen to form the final product - ethanol. The activation energy of this step is 1.01 eV, and the Gibbs free energy is 0.28 eV. For next step, R13, is more favorable. It has a lower activation energy of 0.39 eV and a negative Gibbs free energy is negative of − 0.31 eV, indicating that the final step of the reaction to form ethanol is not only easier but also thermodynamically favorable.

As for water formation, it forms form OH* react with H* in R14, where H* is formed from the dissociation of H_2 (R15). OH* is formed form the reaction between O* and H*(R16), which is kinetically and thermodynamically favorable with a very low activation energy (0.11 eV) and a negative Gibbs free energy (-1.59 eV), making it an extremely favored step along the pathway. All of these reactions show low activation energies and favorable Gibbs free energy.

3.4. Microkinetic modelling

The DFT calculations treat each reaction step independently and do not account for the availability of the reactants. In complex, sequential reaction schemes, they cannot explain the product selectivity well [61]. Thus, a microkinetic model is developed to evaluate the effect of the parameters of individual elementary reactions on the catalytic performance. The both forward and reverse reaction rate for all elementary steps are listed and shown in Table S8. We investigated the mechanistic and (micro)kinetic aspects of this catalytic system as a function of reaction conditions. The hydrogenation of CO_2 to ethanol is an exothermic process that is kinetically controlled, indicating a competition between the thermodynamics (low temperatures for a more favorable equilibrium) and kinetics (high temperature for higher reaction rates) to achieve optimal conversion and selectivity [62].

Reaction temperature is an important factor influencing the selectivity. However, the high temperature required to activate CO_2 in thermal catalysis may trigger carbon deposition (coking), sintering of the catalysts and even catalyst degradation [63]. However, because the hydrogenation of CO_2 to ethanol is an exothermic reaction, a lower temperature is preferred over a higher thermodynamic more favorable conversion that may be kinetically unfavorable. since the activation of CO_2 to CO is an endothermic reaction, therefore, an appropriate reaction temperature not only helps to improve the selectivity of ethanol, but also increases the catalyst activity. The reaction temperature in the real catalytic systems is mostly concentrated in 200–350 °C [56], which are also the temperatures we used in microkinetic modelling. As shown in Fig. 5a, the selectivity of ethanol initially increases with the rising temperature, reaching a peak at 250 °C, after which it begins to decline. Therefore, 250 °C is chosen as the optimal reaction temperature.

The H_2/CO_2 ratio also impacts the reaction. After CO_2 is reduced to CO, the excess H_2 can easily reduce CO to alkanes in a competitive reaction, therefore it is necessary to select an appropriate H_2/CO_2 ratio. In our microkinetic model, the total pressure of the reaction system is maintained at 4 bar, and the temperature is fixed at 250 °C to maintain a high selectivity of ethanol while investigating the effects of varying reactant ratios. As the H_2/CO_2 ratio increases (Fig. 5b), ethanol selectivity improves progressively. As expected from the thermodynamics considerations, a change in selectivity with increasing pressure was observed, as shown in Fig. 5c. While keeping other reaction conditions unchanged, the selectivity of ethanol increases with rising pressure.

Fig. 5d presents the final coverage of products, intermediates, and empty active sites under varying reaction conditions, where only one parameter is changed while maintaining a H_2/CO_2 feed ratio of 3, a reaction temperature of 250 °C, and a total pressure of 4 bar. At the end of this microkinetic model, the active sites are occupied by ethanol, water and other species, such as H*, OH* and CH_3CHO. Fig. 5e–h illustrates the time-dependent evolution of reactant, product, and intermediate species coverage under the same reaction conditions. As shown in Fig. 5e, the adsorption of reactants initiates the reaction, followed by chemical transformations leading to product formation. Fig. 5f highlights key intermediate species with significant coverage, suggesting their major role in facilitating product formation. For completeness, Fig. 5g–h display intermediates with lower coverage, representing transient species or less stable intermediates that appear briefly during the reaction process.

The TOF provides important insights into the relationship between temperature and catalytic efficiency. The apparent activation energy, derived from TOF measurements and plotted against inverse temperature (Fig. 6), show different kinetic behaviors for ethanol (0.39 eV) and methanol (0.27 eV). A higher activation energy corresponds to a stronger temperature dependence of the TOF, which is reflected in the slope of the Arrhenius plot for ethanol [64].

However, under the given reaction conditions in the postulated reactor model, methanol exhibits a higher TOF than ethanol, indicating it is a kinetically favorable product. It should be noted that the TOF values in our batch system are time-dependent. Therefore, the maximum TOF values were used to construct the log (TOF) vs. 1/T plots. The selectivity, on the other hand, was evaluated at the final reaction time (at the end of the simulation). As can be seen in Fig. S7, the maximum production of methanol appears before ethanol, which means that methanol is formed first and then converted to ethanol.

The significantly higher final ethanol selectivity observed in our microkinetic modeling, despite the kinetic advantage of methanol indicates that ethanol formation is thermodynamically favored under these conditions. This is consistent with prior studies demonstrating that ethanol synthesis is preferentially stabilized at equilibrium due to its lower Gibbs free energy (the ΔG for CO_2 hydrogenation to ethanol is − 32.4 kJ/mol, whereas for methanol, it is 3.5 kJ/mol [65]). Thus, the product distribution results from kinetic (TOF-driven) and thermodynamic (equilibrium-driven) factors.

3.5. Comparison with existing models

The goal of theoretical modeling is twofold: it can be used to yield valuable fundamental insights or to describe existing catalysts to

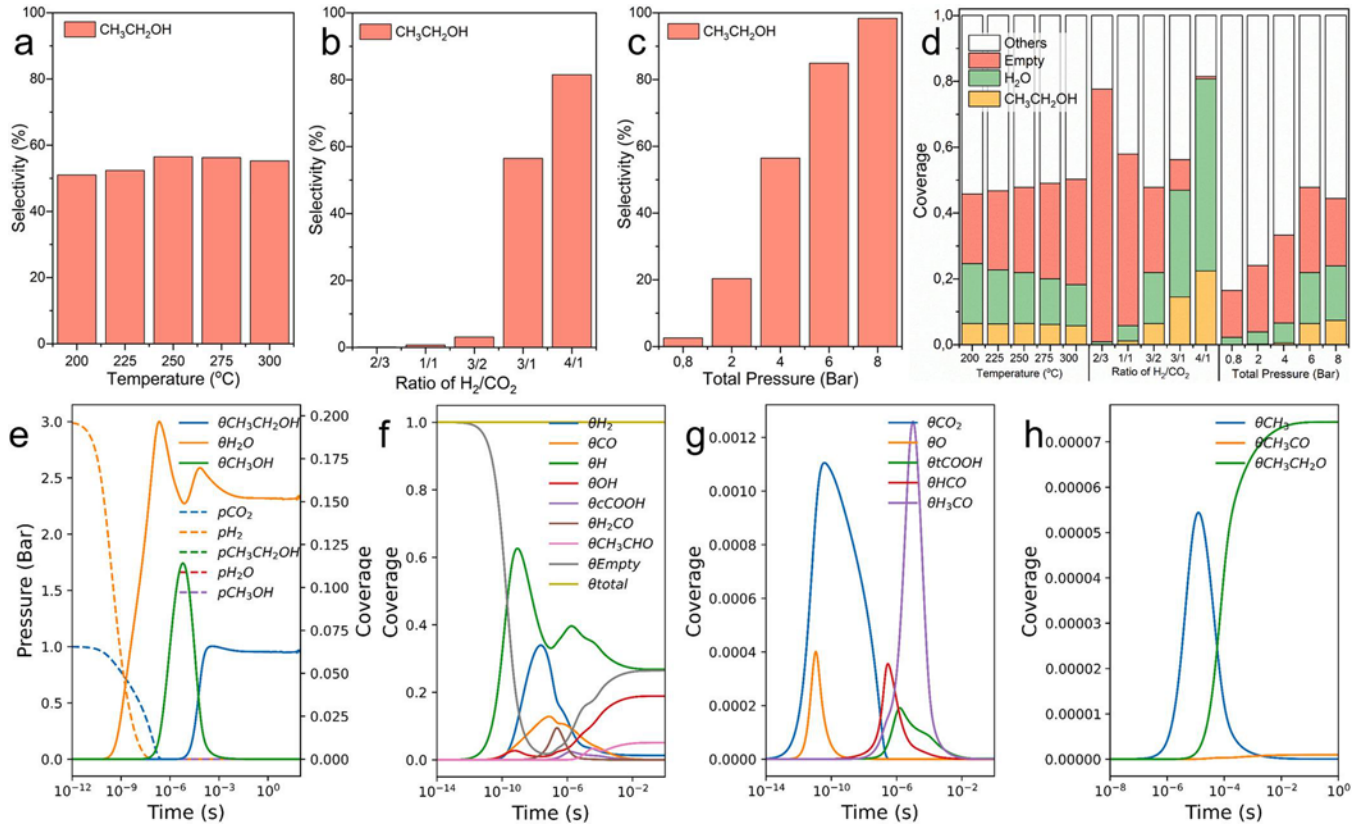

Fig. 5. Selectivity of ethanol: (a) Variation in reaction temperature (H_2/CO_2 feed ratio: 3, total pressure: 4 bar); (b) variation in H_2/CO_2 feed ratio (reaction temperature: 250 °C, total pressure: 4 bar); (c) variation in total pressure (H_2/CO_2 feed ratio: 3, reaction temperature: 250 °C); (d) Final coverage of products and other intermediates, as well as empty actives sites under different reaction conditions (H_2/CO_2 feed ratio: 3, reaction temperature: 250 °C, total pressure: 4 bar, with only one condition changed); (e-h) Time-dependent variations in the coverage of reactants, products, and intermediate species under the same reaction conditions (H_2/CO_2 feed ratio: 3, reaction temperature: 250 °C, total pressure: 4 bar). Conversion of CO_2 and H_2 is 100 % under all reaction conditions.

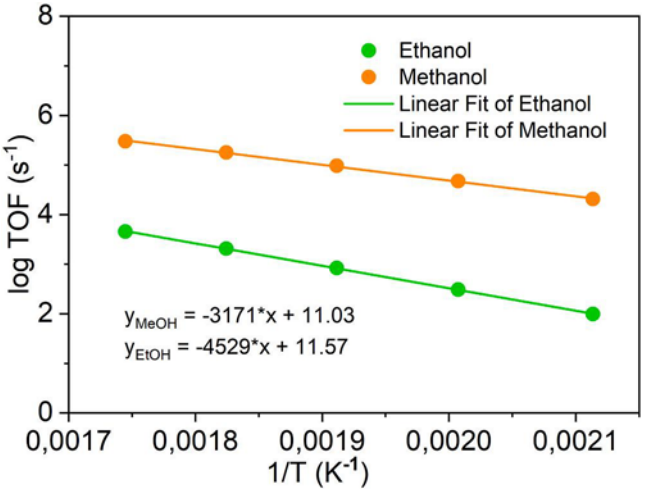

Fig. 6. Arrhenius plot for methanol and ethanol formation in CO_2 hydrogenation. The slope of the Arrhenius plot represents the apparent activation energy, which is determined by the slope of the fitting linear line on the plot. Note that we plot maximum TOFs, which do not occur at the same time for both reactions.

provide and practical recommendations for experimentalists. While different models or approaches will invariably give different predictions, common themes are present. Our primary focus is foremost theoretical but we also aim to bridge the gap between theory and experiments as a secondary goal.

Table 4 shows a short literature of *ab initio* models for the synthesis of ethanol from CO_2 and H_2 on various catalysts, mostly but not limited to Cu. It lists studies that combine both experimental work and DFT calculations, along with the functionals used, model types, and experimental characterization methods to validate the simulated reaction pathways.

Most importantly, the table highlights the C-C coupling mechanism involved, which is crucial for C2 synthesis. Most of these studies postulate the carboxyl mechanism, which is consistently supported by both experimental data and computational results. The detailed catalytic performance of different catalysts under varying reaction conditions for CO_2 hydrogenation to ethanol has already been extensively discussed and summarized [5,78]. Current experimental studies show that the temperatures reported in the literature typically range from 140 °C to 350 °C, with increasing pressure shifts the equilibrium toward ethanol production. The most common feed ratio reported is $H_2/CO_2 = 3$, aligning well with our theoretical predictions.

4. Conclusions

In this study, we utilized density functional theory (DFT) and a microkinetic batch reactor model to investigate the mechanism of ethanol synthesis through CO_2 hydrogenation on a trinuclear Cu-ZSM-5 catalyst. In building the catalyst model, we accounted for the substitution energies of triple copper active sites integrated within the ZSM-5 framework to identify the most probable and stable structure of the trinuclear catalyst. We identified the mechanism of the reaction and that the C-C coupling occurs via the CH_3-CHO step, which has an activation barrier of 0.11 eV.

Table 4
Literature review regarding simulation and experiment for CO_2 hydrogenation to ethanol.

Catalyst	Computational Information		Experiment Characterization methods	C-C Coupling	Ref.
Cu@Na-Beta	VASP (GGA-PBE, DFTD3)	Slab Model	GC-MS; In situ FT-IR; NMR; TPD	$CO_2 + CH_3 \rightarrow CH_3COO$	[10]
Zr_{12}-bpdc-CuCs	Gaussian 09 (B3LYP)	Framework Model	GC-MS; XPS; XANES	$CH_3OH + HCO \rightarrow CH_3CHO$	[7]
$Rh_1/CeTiO_x$	VASP5.4.4 (PBE, DFT+U)	Slab Model	DRIFT; Raman; GC; H NMR	$CH_3 + CO \rightarrow CH_3CO$	[66]
Au Clusters	VASP (GGA-PBE, DFT-D3);	Cluster Model	FT-IR; In situ DRIFT	$CH_2 + CO \rightarrow CH_2CO$	[67]
$Co_{0.52}Ni_{0.48}AlO_x$	Mathematic Modelling		FT-IR; Raman; NMR,	$HCOO + CH_x \rightarrow CH_3COO + C_2H_5O$	[68]
Dual Pd	VASP(GGA-PBE);	Slab Model	FTIR; XANES; H_2-TPR	$CH_3 + CO \rightarrow CH_3CO$	[29]
CoCu	VASP(GGA-BEEF-vdW)	Slab Model,	In situ DRIFT; XPS;	$CH_2 + CO \rightarrow CH_2CO$	[69]
Pd_2/CeO_2	VASP(PBE)	Slab Model	DRIFTS; FTIR; EXAFS;	$CH_3 + CO \rightarrow CH_3CO$	[26]
Na-Fe@C/K-CuZnAl	VASP (GGA-PBE)	Slab Model	XANES; EXAFS; In situ DRIFT;	$CH_m + CO \rightarrow CH_mCO$; $CH_m + CHO \rightarrow CH_mCHO$; $CH_m + CH_xO \rightarrow CH_mCH_xO$; $CH_m + COO \rightarrow CH_mCOO$	[70]
CuBr-DDT	VASP5.4.4 (GGA-PBE, DFTD3)	Slab Model	XPS; FTIR	$CHO + CO \rightarrow COCHO$	[71]
Rh− 0.3VOx/MCM-41	VASP (PBE)	Slab Model	Raman; In situ DRIFTS;	$CH_3 + CO \rightarrow CH_3CO$	[72]
Na-Co_2C	VASP(PBE)	Slab Model	XANES; EXAFS; In situ DRIFTS;	$CH_x + CO \rightarrow CH_xCO$	[73]
Co_2C||CuZnAl	VASP (GGA-PBE, DFTD3)	Structure Model	In situ DRIFTS; FTIR; CTK;	$CH_2 + CHO \rightarrow CH_2CHO$	[74]
PCN-224-Cu	Gaussian 16 (MN15/Def2-TZVP//B3LYP/Def2-SVP)	Molecular Model	FTIR; XPS; In situ DRIFTS;	$CH_3 + CH_2 \rightarrow CH_3CH_2$	[75]
FeNaS	VASP (GGA-PBE)	Slab Model	In situ DRIFTS; XPS;	$CH_x + CO \rightarrow CH_xCO$	[76]
Cu/C	VASP5.3.3 (PBE)	Cluster Model	FTIR; XPS; XANES; EXAFS; Operando XAS	$CH_3 + H_2CO \rightarrow CH_3CH_2O$	[77]

Using the batch model, we determined that the best temperature for maximizing the ethanol selectivity is 250 °C. We also identified an H_2/CO_2 ratio of 3 as optimal when the total pressure of the reaction is 4 bar. These findings suggest that trinuclear Cu-ZSM-5 zeolites hold great promise for applications in hydrocarbon conversion and environmental catalysis, offering improved efficiency and selectivity, while the detailed information on the reaction mechanism is useful for further catalyst optimization

To the best of our knowledge, this is the first multiscale model for ethanol production that uses consistent *ab initio* input data on a trinuclear Cu-ZSM-5 catalyst. Admittedly, experimental results might diverge from the idealized model postulates, which served to elucidate the fundamentals of this reaction and to ascertain the feasibilit of trinuclear Cu-ZSM-5 zeolites. Future research should aim to bring together the experimental observations by adjusting the microkinetic model through fitting.

CRediT authorship contribution statement

Chaomin Chen: Methodology, Formal analysis, Investigation, Data curation, Writing – original draft, Visualization. **Jurij Golobič:** Methodology, Data curation, Investigation, Validation. **Žan Lavrič:** Investigation, Methodology. **Matej Huš:** Conceptualization, Supervision, Methodology, Visualization, Resources, Visualization, Funding acquisition, Writing – review & editing. **Blaž Likozar:** Conceptualization, Supervision, Resources, Funding acquisition.

Declaration of Competing Interest

The authors declare that they have no known competing financial interests or personal relationships that could have appeared to influence the work reported in this paper.

Acknowledgements

This work was financially supported by the Slovenian Research and Innovation Agency through the core programme P2-0152, projects J1-3020 (M.H.), J7-4638 (B.L.) and infrastructure funding I0-0039 (M.H.). Financial support of China Scholarship Council (Project ID: 202208330018) is gratefully acknowledged.

Appendix A. Supporting information

Supplementary data associated with this article can be found in the online version at doi:10.1016/j.apcatb.2025.125429.

Data availability

Data will be made available on request.

References

[1] J. Zhang, C.D. Sewell, H. Huang, Z. Lin, Closing the anthropogenic chemical carbon cycle toward a sustainable future via CO_2 valorization, Adv. Energy Mater. 11 (2021) 1–38, https://doi.org/10.1002/aenm.202102767.
[2] K.A. Oyewole, O.B. Okedere, K.O. Rabiu, K.O. Alawode, S. Oyelami, Carbon dioxide emission, mitigation and storage technologies pathways, Sustain. Environ. 9 (2023) 0–17, https://doi.org/10.1080/27658511.2023.2188760.
[3] J. Gao, S. Choo Sze Shiong, Y. Liu, Reduction of CO_2 to chemicals and fuels: thermocatalysis versus electrocatalysis, Chem. Eng. J. 472 (2023) 145033, https://doi.org/10.1016/j.cej.2023.145033.
[4] M.B.S. Felgueiras, M.F.R. Pereira, O.S.G.P. Soares, Effect of the support on the CO_2 hydrogenation to C_2-C_4 products, Catal. Today 441 (2024) 114900, https://doi.org/10.1016/j.cattod.2024.114900.
[5] X. Li, J. Ke, R. Li, P. Li, Q. Ma, T.S. Zhao, Research progress of hydrogenation of carbon dioxide to ethanol, Chem. Eng. Sci. 282 (2023) 119226, https://doi.org/10.1016/j.ces.2023.119226.
[6] G. Cui, Y. Lou, M. Zhou, Y. Li, G. Jiang, C. Xu, Review of mechanism investigations and catalyst developments for CO_2 hydrogenation to alcohols, Catalysts 14 (2024), https://doi.org/10.3390/catal14040232.
[7] B. An, Z. Li, Y. Song, J. Zhang, L. Zeng, C. Wang, W. Lin, Cooperative copper centres in a metal–organic framework for selective conversion of CO_2 to ethanol, Nat. Catal. 2 (2019) 709–717, https://doi.org/10.1038/s41929-019-0308-5.
[8] D. Karapinar, C.E. Creissen, J.G. Rivera De La Cruz, M.W. Schreiber, M. Fontecave, Electrochemical CO_2 reduction to ethanol with copper-based catalysts, ACS Energy Lett. 6 (2021) 694–706, https://doi.org/10.1021/acsenergylett.0c02610.
[9] Z.P. Hu, J. Han, Y. Wei, Z. Liu, Dynamic evolution of zeolite framework and metal-zeolite interface, ACS Catal. 12 (2022) 5060–5076, https://doi.org/10.1021/acscatal.2c01233.
[10] L. Ding, T. Shi, J. Gu, Y. Cui, Z. Zhang, C. Yang, T. Chen, M. Lin, P. Wang, N. Xue, L. Peng, X. Guo, Y. Zhu, Z. Chen, W. Ding, CO_2 Hydrogenation to ethanol over Cu@Na-beta, Chem 6 (2020) 2673–2689, https://doi.org/10.1016/j.chempr.2020.07.001.
[11] M.L. Tsai, R.G. Hadt, P. Vanelderen, B.F. Sels, R.A. Schoonheydt, E.I. Solomon, $[Cu_2O]^{2+}$ Active site formation in Cu-ZSM-5: geometric and electronic structure requirements for N_2O activation, J. Am. Chem. Soc. 136 (2014) 3522–3529, https://doi.org/10.1021/ja4113808.
[12] G. Li, P. Vassilev, M. Sanchez-Sanchez, J.A. Lercher, E.J.M. Hensen, E.A. Pidko, Stability and reactivity of copper oxo-clusters in ZSM-5 zeolite for selective

methane oxidation to methanol, J. Catal. 338 (2016) 305–312, https://doi.org/10.1016/j.jcat.2016.03.014.
[13] M.H. Mahyuddin, A. Staykov, Y. Shiota, M. Miyanishi, K. Yoshizawa, Roles of zeolite confinement and Cu-O-Cu angle on the direct conversion of methane to methanol by $[Cu_2(\mu\text{-}O)]^{2+}$-exchanged AEI, CHA, AFX, and MFI zeolites, ACS Catal. 7 (2017) 3741–3751, https://doi.org/10.1021/acscatal.7b00588.
[14] Y. Li, S.H. Chan, Q. Sun, Heterogeneous catalytic conversion of CO_2: a comprehensive theoretical review, Nanoscale 7 (2015) 8663–8683, https://doi.org/10.1039/c5nr00092k.
[15] S. Zhang, Z. Wu, X. Liu, K. Hua, Z. Shao, B. Wei, C. Huang, H. Wang, Y. Sun, A short review of recent advances in direct CO_2 hydrogenation to alcohols, Top. Catal. 64 (2021) 371–394, https://doi.org/10.1007/s11244-020-01405-w.
[16] S. Grundner, M.A.C. Markovits, G. Li, M. Tromp, E.A. Pidko, E.J.M. Hensen, A. Jentys, M. Sanchez-Sanchez, J.A. Lercher, Single-site trinuclear copper oxygen clusters in mordenite for selective conversion of methane to methanol, Nat. Commun. 6 (2015) 1–9, https://doi.org/10.1038/ncomms8546.
[17] Y.J. Son, D. Kim, J.W. Park, K. Ko, Y. Yu, S.J. Hwang, Heteromultimetallic platform for enhanced C–H bond activation: aluminum-incorporated dicopper complex mimicking Cu-ZSM-5 structure and oxidative reactivity, J. Am. Chem. Soc. (2024), https://doi.org/10.1021/jacs.4c11614.
[18] M.H. Groothaert, P.J. Smeets, B.F. Sels, P.A. Jacobs, R.A. Schoonheydt, Selective oxidation of methane by the bis(μ-oxo) dicopper core stabilized on ZSM-5 and mordenite zeolites, J. Am. Chem. Soc. 127 (2005) 1394–1395, https://doi.org/10.1021/ja047158u.
[19] G. Brezicki, J. Zheng, C. Paolucci, R. Schlögl, R.J. Davis, Effect of the Co-cation on Cu speciation in Cu-exchanged mordenite and ZSM-5 catalysts for the oxidation of methane to methanol, ACS Catal. 11 (2021) 4973–4987, https://doi.org/10.1021/acscatal.1c00543.
[20] C. Gao, J. Li, J. Zhang, X. Sun, DFT study on the combined catalytic removal of N_2O, NO, and NO_2 over binuclear Cu-ZSM-5, Catalysts 12 (2022), https://doi.org/10.3390/catal12040438.
[21] C. Dai, Y. Zhang, N. Liu, G. Yu, N. Wang, R. Xu, B. Chen, Mechanistic insight into the effect of active site motif structures on direct oxidation of methane to methanol over Cu-ZSM-5, Phys. Chem. Chem. Phys. (2023) 24894–24903, https://doi.org/10.1039/d3cp01906c.
[22] X. Ma, M. Li, M. Lei, Trinuclear transition metal complexes in catalytic reactions, Acta Chim. Sin. 81 (2023) 84–99, https://doi.org/10.6023/A22100425.
[23] S. Grundner, M.A.C. Markovits, G. Li, M. Tromp, E.A. Pidko, E.J.M. Hensen, A. Jentys, M. Sanchez-Sanchez, J.A. Lercher, Single-site trinuclear copper oxygen clusters in mordenite for selective conversion of methane to methanol, Nat. Commun. 6 (2015) 1–9, https://doi.org/10.1038/ncomms8546.
[24] M. Dong, Q. Pan, F. Meng, X. Yao, S. You, G. Shan, C. Sun, X. Wang, Z. Su, Trinuclear Cu-based covalent organic framework: π-conjugated framework regulating electron delocalization to promote photoreduction CO_2, J. Colloid Interface Sci. 662 (2024) 807–813, https://doi.org/10.1016/j.jcis.2024.02.129.
[25] Y. Wang, W. Wang, R. He, M. Li, J. Zhang, F. Cao, J. Liu, S. Lin, X. Gao, G. Yang, M. Wang, T. Xing, T. Liu, Q. Liu, H. Hu, N. Tsubaki, M. Wu, Carbon-based electron buffer layer on ZnO_x−Fe_5C_2−Fe_3O_4 boosts ethanol synthesis from CO_2 hydrogenation, Angew. Chem. - Int. Ed. 62 (2023), https://doi.org/10.1002/anie.202311786.
[26] Y. Lou, F. jiang, W. Zhu, L. Wang, T. Yao, S. Wang, B. Yang, B. Yang, Y. Zhu, X. Liu, CeO_2 supported Pd dimers boosting CO_2 hydrogenation to ethanol, Appl. Catal. B Environ. 291 (2021) 120122, https://doi.org/10.1016/j.apcatb.2021.120122.
[27] P. Xie, J. Ding, Z. Yao, T. Pu, P. Zhang, Z. Huang, C. Wang, J. Zhang, N. Zecher-Freeman, H. Zong, D. Yuan, S. Deng, R. Shahbazian-Yassar, C. Wang, Oxo dicopper anchored on carbon nitride for selective oxidation of methane, Nat. Commun. 13 (2022) 1–10, https://doi.org/10.1038/s41467-022-28987-1.
[28] C. Paolucci, I. Khurana, A.A. Parekh, S. Li, A.J. Shih, H. Li, J.R. Di Iorio, J. D. Albarracin-caballero, A. Yezerets, J.T. Miller, W.N. Delgass, F.H. Ribeiro, W. F. Schneider, R. Gounder, Dynamic multinuclear sites formed by mobilized copper ions in NO_x selective catalytic reduction, Science 357 (2017) 898–903, https://doi.org/10.1126/science.aan5630.
[29] J. Chen, Y. Zha, B. Liu, Y. Li, Y. Xu, X. Liu, Rationally designed water enriched nano reactor for stable CO_2 hydrogenation with near 100 % ethanol selectivity over diatomic palladium active sites, ACS Catal. (2023) 7110–7121, https://doi.org/10.1021/acscatal.3c00586.
[30] H. Ding, J. Zhang, W. Feng, Q. Yao, L. Zhang, Y. Ren, L. Ye, B. Yue, H. He, Precise confinement and position distribution of atomic Cu and Zn in ZSM-5 for CO_2 hydrogenation to methanol, Nanomaterials 13 (2023), https://doi.org/10.3390/nano13233053.
[31] X. Tang, Z. Liu, L. Huang, W. Chen, C. Li, G. Wang, G. Li, X. Yi, A. Zheng, Violation or abidance of Löwenstein's rule in zeolites under synthesis conditions? ACS Catal. 9 (2019) 10618–10625, https://doi.org/10.1021/acscatal.9b01844.
[32] J. Enkovaara, C. Rostgaard, J.J. Mortensen, J. Chen, M. Dułak, L. Ferrighi, J. Gavnholt, C. Glinsvad, V. Haikola, H.A. Hansen, H.H. Kristoffersen, M. Kuisma, A.H. Larsen, L. Lehtovaara, M. Ljungberg, O. Lopez-Acevedo, P.G. Moses, J. Ojanen, T. Olsen, V. Petzold, N.A. Romero, J. Stausholm-Møller, M. Strange, G. A. Tritsaris, M. Vanin, M. Walter, B. Hammer, H. Häkkinen, G.K.H. Madsen, R. M. Nieminen, J.K. Nørskov, M. Puska, T.T. Rantala, J. Schiøtz, K.S. Thygesen, K. W. Jacobsen, Electronic structure calculations with GPAW: a real-space implementation of the projector augmented-wave method, J. Phys. Condens. Matter 22 (2010), https://doi.org/10.1088/0953-8984/22/25/253202.
[33] J.J. Mortensen, L.B. Hansen, K.W. Jacobsen, Real-space grid implementation of the projector augmented wave method, Phys. Rev. B - Condens. Matter Mater. Phys. 71 (2005) 1–11, https://doi.org/10.1103/PhysRevB.71.035109.
[34] S.R. Bahn, K.W. Jacobsen, An object-oriented scripting interface to a legacy electronic structure code, Comput. Sci. Eng. 4 (2002) 56–66, https://doi.org/10.1109/5992.998641.
[35] J.P. Perdew, K. Burke, M. Ernzerhof, Generalized gradient approximation made simple, Phys. Rev. Lett. 77 (1996) 3865–3868, https://doi.org/10.1103/PhysRevLett.77.3865.
[36] S. Grimme, J. Antony, S. Ehrlich, H. Krieg, A consistent and accurate ab initio parametrization of density functional dispersion correction (DFT-D) for the 94 elements H-Pu, J. Chem. Phys. 132 (2010), https://doi.org/10.1063/1.3382344.
[37] B. Mounssef, S.F. de Alcântara Morais, A.P. de Lima Batista, L.W. de Lima, A.A. C. Braga, DFT study of H_2 adsorption at a Cu-SSZ-13 zeolite: a cluster approach, Phys. Chem. Chem. Phys. 23 (2021) 9980–9990, https://doi.org/10.1039/d1cp00422k.
[38] J.D. Head, M.C. Zerner, A Broyden-Fletcher-Goldfarb-Shanno optimization procedure for molecular geometries, Chem. Phys. Lett. 122 (1985) 264–270, https://doi.org/10.1016/0009-2614(85)80574-1.
[39] G. Mills, H. Jónsson, G.K. Schenter, Reversible work transition state theory: application to dissociative adsorption of hydrogen, Surf. Sci. 324 (1995) 305–337, https://doi.org/10.1016/0039-6028(94)00731-4.
[40] M. He, J. Zhang, X.L. Sun, B.H. Chen, Y.G. Wang, Theoretical study on methane oxidation catalyzed by Fe/ZSM-5: the significant role of water on binuclear iron active sites, J. Phys. Chem. C 120 (2016) 27422–27429, https://doi.org/10.1021/acs.jpcc.6b09548.
[41] K. Momma, F. Izumi, VESTA 3 for three-dimensional visualization of crystal, volumetric and morphology data, J. Appl. Crystallogr 44 (2011) 1272–1276, https://doi.org/10.1107/S0021889811038970.
[42] H.G, A.H. Unni Engedahl, Adam A. Arvidsson, Reaction mechanism for methane-to-methanol in CU-SSZ-13: first-principles study of the $Z_2[Cu_2O]$ and $Z_2[Cu_2OH]$ Motifs, Catalysts 11 (2021) 1–12, https://doi.org/10.3390/catal11010017.
[43] G.R. Wittreich, K. Alexopoulos, D.G. Vlachos, Microkinetic modeling of surface catalysis. Handb. Mater. Model. Appl. Curr. Emerg. Mater., Second Ed., 2020, pp. 1377–1404 (⟨https://doi.org/10.1007/978-3-319-44680-6_5⟩).
[44] X. Nie, X. Jiang, H. Wang, W. Luo, M.J. Janik, Y. Chen, X. Guo, C. Song, Mechanistic understanding of alloy effect and water promotion for Pd-Cu bimetallic catalysts in CO_2 hydrogenation to methanol, ACS Catal. 8 (2018) 4873–4892, https://doi.org/10.1021/acscatal.7b04150.
[45] U. Engedahl, A. Boje, H. Ström, H. Grönbeck, A. Hellman, Complete reaction cycle for methane-to-methanol conversion over Cu-SSZ-13: first-principles calculations and microkinetic modeling, J. Phys. Chem. C 125 (2021) 14681–14688, https://doi.org/10.1021/acs.jpcc.1c04062.
[46] Database of Zeolite Structures, ⟨http://www.iza-structure.org/databases/⟩, 2023 (Accessed 14 March 2023).
[47] S.R. Bare, S.D. Kelly, W. Sinkler, J.J. Low, F.S. Modica, S. Valencia, A. Corma, L. T. Nemeth, Uniform catalytic site in Sn-β-zeolite determined using X-ray absorption fine structure, J. Am. Chem. Soc. 127 (2005) 12924–12932, https://doi.org/10.1021/ja052543k.
[48] X. Tang, J. Ye, L. Guo, T. Pu, L. Cheng, X.M. Cao, Y. Guo, L. Wang, Y. Guo, W. Zhan, S. Dai, Atomic insights into the Cu species supported on zeolite for direct oxidation of methane to methanol via low-damage HAADF-STEM, Adv. Mater. 2208504 (2023) 1–9, https://doi.org/10.1002/adma.202208504.
[49] X. Liu, J. Zhang, C. Huang, X. Sun, Density functional theory study of Cu-ZSM-5-catalyzed C–H bond activation: the importance of active centers, J. Phys. Chem. C 122 (2018) 28645–28651, https://doi.org/10.1021/acs.jpcc.8b08137.
[50] J. Dědeček, L. Čapek, B. Wichterlová, Nature of active sites in decane-SCR-NO_x and NO decomposition over Cu-ZSM-5 zeolites, Appl. Catal. A Gen. 307 (2006) 156–164, https://doi.org/10.1016/j.apcata.2006.03.017.
[51] K.M. Farhan, A.N.K. Thabassum, T.M. Ismail, P.K. Sajith, Theoretical investigation into the effect of water on the N_2O decomposition reaction over the Cu-ZSM-5 catalyst, Catal. Sci. Technol. 12 (2022) 1466–1475, https://doi.org/10.1039/d1cy01883c.
[52] J.S. Woertink, P.J. Smeets, M.H. Groothaert, M.A. Vance, B.F. Sels, R. A. Schoonheydt, E.I. Solomon, A $[Cu_2O]^{2+}$ core in Cu-ZSM-5, the active site in the oxidation of methane to methanol, Proc. Natl. Acad. Sci. USA 106 (2009) 18908–18913, https://doi.org/10.1073/pnas.0910461106.
[53] P. Vanelderen, J. Vancauwenbergh, B.F. Sels, R.A. Schoonheydt, Coordination chemistry and reactivity of copper in zeolites, Coord. Chem. Rev. 257 (2013) 483–494, https://doi.org/10.1016/j.ccr.2012.07.008.
[54] L. Vilella, F. Studt, The stability of copper oxo species in zeolite frameworks, Eur. J. Inorg. Chem. 2016 (2016) 1514–1520, https://doi.org/10.1002/ejic.201501270.
[55] M. Huš, V.D.B.C. Dasireddy, N. Strah Štefančič, B. Likozar, Mechanism, kinetics and thermodynamics of carbon dioxide hydrogenation to methanol on $Cu/ZnAl_2O_4$ spinel-type heterogeneous catalysts, Appl. Catal. B Environ. 207 (2017) 267–278, https://doi.org/10.1016/j.apcatb.2017.01.077.
[56] S.S. Ali, S.S. Ali, N. Tabassum, A review on CO_2 hydrogenation to ethanol: reaction mechanism and experimental studies, J. Environ. Chem. Eng. 10 (2022) 106962, https://doi.org/10.1016/j.jece.2021.106962.
[57] F. Zeng, C. Mebrahtu, X. Xi, L. Liao, J. Ren, J. Xie, H.J. Heeres, R. Palkovits, Catalysts design for higher alcohols synthesis by CO_2 hydrogenation: trends and future perspectives, Appl. Catal. B Environ. 291 (2021) 120073, https://doi.org/10.1016/j.apcatb.2021.120073.
[58] X. Zheng, L. Guo, W. Li, Z. Cao, N. Liu, Q. Zhang, M. Xing, Y. Shi, J. Guo, Insight into the mechanism of reverse water-gas shift reaction and ethanol formation catalyzed by Mo_6S_8-TM clusters, Mol. Catal. 439 (2017) 155–162, https://doi.org/10.1016/j.mcat.2017.06.030.

[59] H. Zheng, R. Zhang, Z. Li, B. Wang, Insight into the mechanism and possibility of ethanol formation from syngas on Cu (1 0 0) surface, J. Mol. Catal. A Chem. 404–405 (2015) 115–130, https://doi.org/10.1016/j.molcata.2015.04.015.
[60] X. Zu, Y. Zhao, X. Li, R. Chen, W. Shao, L. Li, P. Qiao, W. Yan, Y. Pan, Q. Xu, J. Zhu, Y. Sun, Y. Xie, Reversible switching Cu_{II}/Cu_{I} single sites catalyze high-rate and selective CO_2 photoreduction, Angew. Chem. - Int. Ed. 62 (2023), https://doi.org/10.1002/anie.202215247.
[61] X. Wang, J. Pan, H. Wei, W. Li, J. Zhao, Z. Hu, Mechanism of methanol synthesis from CO_2 hydrogenation over Pt_8/In_2O_3 catalysts: a combined study on density functional theory and microkinetic modeling, J. Phys. Chem. C 126 (2022) 1761–1769, https://doi.org/10.1021/acs.jpcc.1c08098.
[62] J.J. Spivey, A. Egbebi, Heterogeneous catalytic synthesis of ethanol from biomass-derived syngas, Chem. Soc. Rev. 36 (2007) 1514–1528, https://doi.org/10.1039/b414039g.
[63] N. Zou, J. Chen, T. Qiu, Y. Zheng, Direct hydrogenation of CO_2 to ethanol at ambient conditions using Cu(i)-MOF in a dielectric barrier discharge plasma reactor, J. Mater. Chem. A 11 (2023) 10766–10775, https://doi.org/10.1039/d3ta00314k.
[64] M. Huš, D. Kopač, B. Likozar, Catalytic hydrogenation of carbon dioxide to methanol: synergistic effect of bifunctional Cu/perovskite catalysts, ACS Catal. 9 (2019) 105–116, https://doi.org/10.1021/acscatal.8b03810.
[65] R. Salami, Y. Zeng, X. Han, S. Rohani, Y. Zheng, Exploring catalyst developments in heterogeneous CO_2 hydrogenation to methanol and ethanol: A journey through reaction pathways, J. Energy Chem. 101 (2025) 345–384, https://doi.org/10.1016/j.jechem.2024.08.069.
[66] K. Zheng, Y. Li, B. Liu, F. Jiang, Y. Xu, X. Liu, Ti-doped CeO_2 stabilized single-atom rhodium catalyst for selective and stable CO_2 hydrogenation to ethanol, Angew. Chem. - Int. Ed. 61 (2022), https://doi.org/10.1002/anie.202210991.
[67] D. Yang, W. Pei, S. Zhou, J. Zhao, W. Ding, Y. Zhu, Controllable conversion of CO_2 on non-metallic gold clusters, Angew. Chem. - Int. Ed. 59 (2020) 1919–1924, https://doi.org/10.1002/anie.201913635.
[68] L. Wang, S. He, L. Wang, Y. Lei, X. Meng, F.S. Xiao, Cobalt-nickel catalysts for selective hydrogenation of carbon dioxide into ethanol, ACS Catal. 9 (2019) 11335–11340, https://doi.org/10.1021/acscatal.9b04187.
[69] S. Liu, C. Yang, S. Zha, D. Sharapa, F. Studt, Z. Zhao, J. Gong, Moderate surface segregation promotes selective ethanol production in CO_2 hydrogenation reaction over CoCu catalysts, Angew. Chem. 134 (2022), https://doi.org/10.1002/ange.202109027.
[70] Y. Wang, K. Wang, B. Zhang, X. Peng, X. Gao, G. Yang, H. Hu, M. Wu, N. Tsubaki, Direct conversion of CO_2 to ethanol boosted by intimacy-sensitive multifunctional catalysts, ACS Catal. 11 (2021) 11742–11753, https://doi.org/10.1021/acscatal.1c01504.
[71] J. Wang, H. Yang, Q. Liu, Q. Liu, X. Li, X. Lv, T. Cheng, H. Bin Wu, Fastening Br-ions at copper-molecule interface enables highly efficient electroreduction of CO_2 to ethanol, ACS Energy Lett. 6 (2021) 437–444, https://doi.org/10.1021/acsenergylett.0c02364.
[72] G. Wang, R. Luo, C. Yang, J. Song, C. Xiong, H. Tian, Z.J. Zhao, R. Mu, J. Gong, Active sites in CO_2 hydrogenation over confined VO_x-Rh catalysts, Sci. China Chem. 62 (2019) 1710–1719, https://doi.org/10.1007/s11426-019-9590-6.
[73] S. Zhang, Z. Wu, X. Liu, Z. Shao, L. Xia, L. Zhong, H. Wang, Y. Sun, Tuning the interaction between Na and Co_2C to promote selective CO_2 hydrogenation to ethanol, Appl. Catal. B Environ. 293 (2021) 120207, https://doi.org/10.1016/j.apcatb.2021.120207.
[74] S. Zhang, C. Huang, Z. Shao, H. Zhou, J. Chen, L. Li, J. Lu, X. Liu, H. Luo, L. Xia, H. Wang, Y. Sun, Revealing and regulating the complex reaction mechanism of CO_2 hydrogenation to higher alcohols on multifunctional tandem catalysts, ACS Catal. 13 (2023) 3055–3065, https://doi.org/10.1021/acscatal.2c06245.
[75] S.C. Qi, Z.H. Yang, R.R. Zhu, X.J. Lu, D.M. Xue, X.Q. Liu, L.B. Sun, The cascade catalysis of the porphyrinic zirconium metal-organic framework PCN-224-Cu for CO_2 conversion to alcohols, J. Mater. Chem. A 9 (2021) 24510–24516, https://doi.org/10.1039/d1ta06950k.
[76] R. Yao, J. Wei, Q. Ge, J. Xu, Y. Han, Q. Ma, H. Xu, J. Sun, Monometallic iron catalysts with synergistic Na and S for higher alcohols synthesis via CO_2 hydrogenation, Appl. Catal. B Environ. 298 (2021) 120556, https://doi.org/10.1016/j.apcatb.2021.120556.
[77] H. Xu, D. Rebollar, H. He, L. Chong, Y. Liu, C. Liu, C.J. Sun, T. Li, J.V. Muntean, R. E. Winans, D.J. Liu, T. Xu, Highly selective electrocatalytic CO_2 reduction to ethanol by metallic clusters dynamically formed from atomically dispersed copper, Nat. Energy 5 (2020) 623–632, https://doi.org/10.1038/s41560-020-0666-x.
[78] Q. Zhang, S. Wang, M. Dong, J. Wang, W. Fan, Recent advances in CO_2 hydrogenation to higher alcohols, Sci. China Chem. (2024), https://doi.org/10.1007/s11426-024-2254-x.